

**CHARACTERIZATION OF POROUS SILICON
AND ZINC OXIDE/POROUS SILICON FOR
PHOTODETECTOR APPLICATION**

NURIZATI BINTI ROSLI

UNIVERSITI SAINS MALAYSIA

2018

**CHARACTERIZATION OF POROUS SILICON
AND ZINC OXIDE/POROUS SILICON FOR
PHOTODETECTOR APPLICATION**

by

NURIZATI BINTI ROSLI

Thesis submitted in fulfilment of requirements

for the degree of

Master of Science

September 2018

ACKNOWLEDGEMENT

I would like to thank Allah for granting me good health to complete this research. I want to express appreciation to my supervisor Dr. Mohd Mahadi Halim for suggesting the topic of the thesis, continuous advice, and guidance through this work. Without your support, this thesis would not have been completed. Particularly, you open a new door for me to look up into the physics world. It is my honour to be your student and I am proud of it. I wish to thanks to my co-supervisor, Prof. Dr. Md Roslan Hashim for his supervision. I am totally indebted to the short-term grant 304/PFIZIK/6313095 for partially supporting the raw material of this work.

My thanks are extended to the staffs of the Nano-Optoelectronics Research & Technology Laboratory (NOR Lab) and the Solid-State Laboratory, especially Mrs. Ee Bee Choo, Mr. Abdul Jamil Yusuf, and Mr. Yushamdan Yusof, for their courage and help me to handle the lab works. I would like to express thank you to School of Physics for support financial and giving the opportunity to me presenting in the 6th International Conference on Solid State Science and Technology (ICSSST 2017).

My deepest appreciations are expressed to my lovely father, Mr. Rosli Abu Bakar and lovely mother, Mrs. Siti Fazlina Abdullah for their moral and full financial support for the degree of Master of Science. For all the siblings (Syafiq, Atikah, Syamil, and Syahir), thank you for the continues love and support. Thank you for always being there! I love you all, Lillahita'ala!

My thankful are extended to Mr. Omar, Akram Zaki, Norfazira Mohd Rofi, Izazi Tazri and to all the friends for their continuous help and motivation in this study.

TABLE OF CONTENTS

ACKNOWLEDGEMENT	ii
TABLE OF CONTENTS	iii
LIST OF TABLES	viii
LIST OF FIGURES	x
LIST OF SYMBOLS	xix
LIST OF ABBREVIATIONS	xxi
ABSTRAK	xxiii
ABSTRACT	xxv
CHAPTER 1 - INTRODUCTION	1
1.1 Introduction	1
1.2 Background	1
1.3 Problem Statement	3
1.4 Research Objectives	5
1.5 Research Hypothesis	5
1.6 Scope of The Study	7
1.7 Thesis Organization	8
CHAPTER 2 - LITERATURE REVIEW	9
2.1 Introduction	9
2.2 Introduction to Porous Silicon	9
2.2.1 Basic Properties of Silicon	10
2.2.2 Background of Porous Silicon	13
2.2.3 Structure of Porous Silicon	13

2.2.4 Growth Mechanism of Porous Silicon	15
2.2.5 Structural Properties of Porous Silicon	16
2.2.6 Optical Properties of Porous Silicon	19
2.3 Introduction of ZnO	23
2.3.1 Background of ZnO	23
2.3.2 Crystal structure of ZnO	23
2.3.3 Electronic Properties of ZnO	26
2.3.4 Optical Properties of ZnO	27
2.4 Growth of ZnO on Porous Silicon	28
2.4.1 Growth Technique using Chemical Bath Deposition	28
2.4.2 Growth Mechanism using Chemical Bath Deposition	30
2.4.3 Structural Properties of Growth of ZnO on Porous Silicon	31
2.4.4 Electronic Properties of Growth of ZnO on Porous Silicon	33
2.4.5 Optical Properties of Growth of ZnO on Porous Silicon	34
2.5 Introduction of MSM Photodetector	35
2.5.1 Background of MSM Photodetector	36
2.5.2 Mechanism of Photodetection	38
2.5.3 Zinc Oxide on Porous Silicon for an MSM Photodetector	39
2.5.4 Porous Silicon as an MSM Photodetector	40
2.6 Summary	41
CHAPTER 3 - METHODOLOGY AND INSTRUMENTS	42
3.1 Introduction	42
3.2 Preparation of Porous Silicon	44
3.2.1 Substrates Preparation	44

3.2.2 Radio Corporation of America Cleaning	45
3.2.3 Electrochemical Etching	46
3.3 Growth of ZnO on PS	49
3.3.1 Deposition of ZnO Seed Layer	49
3.3.2 Annealing	51
3.3.3 Chemical Bath Deposition Technique	53
3.4 Thermal Evaporator	55
3.5 Characterization Tools	57
3.5.1 Field Effect Scanning Electron Microscopy and EDX	57
3.5.2 Raman Spectroscopy	60
3.5.3 X-Ray Diffractometer	62
3.5.4 Atomic Force Microscopy	66
3.5.5 UV-Vis Spectroscopy	68
3.5.6 Current-Voltage Measurement	70
3.6 Summary	73
CHAPTER 4 - RESULT AND DISCUSSIONS	74
4.1 Introduction	74
4.2 Effect of etching time on the porosity of Si (100).	75
4.2.1 Weight Loss	75
4.2.2 FESEM and EDX Analysis of Different Etching Time of PS	77
4.2.3 Atomic Force Microscopy Analysis on Different Etching Time	80
4.2.4 X-Ray Diffraction Analysis on Different Etching Time	81
4.2.5 Raman Spectroscopy Analysis on Different Etching Time	83
4.2.6 UV-Vis Spectroscopy Analysis on Different Etching Time	85

4.3 Effect of Different Current on The Porosity of n-Si (100)	89
4.3.1 Weight Loss	89
4.3.2 FESEM and EDX Analysis of Different Current	91
4.3.3 Atomic Force Microscopy Analysis of Different Current	94
4.3.4 X-Ray Diffraction Analysis of Different Current	95
4.3.5 Raman Spectroscopy Analysis of Different Current	97
4.3.6 UV-Vis Spectroscopy Analysis of Different Current	98
4.4 Characterization of ZnO Seed Layer on PS using RF Sputtering	101
4.4.1 FESEM Analysis of Different ZnO Seed Layer Thickness	101
4.4.2 Raman Analysis of Different ZnO Seed Layer Thickness	103
4.4.3 UV-Vis Analysis on Different ZnO Seed Layer Thickness	104
4.5 Growth and Characterization of ZnO on PS	107
4.5.1 FESEM and EDX Analysis on the Growth of ZnO on PS	108
4.5.2 X-Ray Diffraction Analysis on the Growth of ZnO on PS	113
4.5.3 Raman Analysis on the Growth of ZnO on PS	117
4.5.4 UV-Vis analysis on the Growth of ZnO on PS	120
4.6 Fabrication of MSM Photodetector	127
4.6.1 Current-Voltage measurement	128
4.6.2 Responsivity	132
4.6.3 Sensitivity	136
4.6.4 Photoresponse, Rise and Fall Times	139
4.7 Summary	143

CHAPTER 5 - CONCLUSION AND FUTURE WORK	145
5.1 Conclusion	145
5.2 Recommendation for Future Research	147
REFERENCES	148
APPENDICES	
LIST OF PUBLICATION	

LIST OF TABLES

		Page
Table 2.1	Basic information and properties of silicon [19,21,22].	11
Table 2.2	IUPAC recommended the universal of classification of pore size distributions conjunction with electron microscopy data by representing the average percentage of porosity [31].	14
Table 2.3	Description of PS layer formation and growth mechanism due to dissolution chemistry of silicon anodically biased in hydrofluoric acid [34,35].	15
Table 2.4	Work function of different type of metal [72,73,74].	36
Table 2.5	Type of semiconductors and the work function of the contacts [76].	37
Table 3.1	Short description of wafer cleaning solution using RCA [87].	45
Table 4.1	Details of PS with different etching time of (5, 10, 15, and 20) minutes and weight loss at constant current flow of 25 mA using solution of HF and ethanol in ratio of 1:4.	76
Table 4.2	Details of FESEM and EDX analysis of PS with different etching time of (5, 10, 15, and 20) minutes at constant current flow of 25 mA, using solution of HF and ethanol in ratio of 1:4.	79
Table 4.3	XRD analysis of PS1, PS2, PS3 and PS4 with different etching time of (5, 10, 15, and 20) minutes at constant current flow of 25 mA and using solution of HF and ethanol in ratio of 1:4.	82
Table 4.4	Data of energy gap of the samples from the extrapolation of a straight line of Tauc's plot for PS1, PS2, PS3 and PS4 using different etching time of (5, 10, 15, and 20) minutes at constant current flow of 25 mA and using solution of HF and ethanol in ratio of 1:4.	87
Table 4.5	Details of PS5, PS6, PS7 and PS8 with different current of (10, 15, 20, and 25) mA at constant etching time of 15 minutes and using solution of HF and ethanol in ratio of 1:4.	90

Table 4.6	Details of FESEM and EDX analysis of PS5, PS6, PS7, and PS8 with different current of (10, 15, 20, and 25) mA at constant etching time of 15 minutes and using solution of HF and ethanol in ratio of 1:4.	93
Table 4.7	XRD analysis of PS5, PS6, PS7, and PS8 using different current of (10, 15, 20, and 25) mA at constant etching time of 15 minutes and using solution of HF and ethanol in ratio of 1:4.	96
Table 4.8	Data of energy gap of the samples for PS5, PS6, PS7, and PS8 using different current of (10, 15, 20, and 25) mA at constant etching time of 15 minutes and using solution of HF and ethanol in ratio of 1:4.	100
Table 4.9	Energy gap between the samples of the different thickness of the ZnO _{seed layer} /PS, a) thickness ZnO seed layer of 50 nm, b) thickness ZnO seed layer of 100 nm and c) thickness ZnO seed layer of 200 nm.	105
Table 4.10	Details of the samples of ZnO _{CBD} /ZnO _{seed layer} /PS using different seed layer thickness, with increasing CBD growth durations for (1, 3 and 5) hours.	107
Table 4.11	Details of FESEM and EDX analysis of the ZnO _{CBD} /ZnO _{seed layer} /PS.	112
Table 4.12	XRD analysis of the ZnO _{CBD} /ZnO _{seed layer} /PS.	116
Table 4.13	Raman analysis of the ZnO _{CBD} /ZnO _{seed layer} /PS.	119
Table 4.14	Data of energy gap of the ZnO _{CBD} /ZnO _{seed layer} /PS.	124
Table 4.15	<i>I-V</i> measurements on MSM photodetectors.	131
Table 4.16	Rise and decay time of MSM photodetectors.	142
Table 4.17	The values of non-annealed MSM photodetector in this work and obtained from the reported of the ZnO nanorods on PS photodetectors [12,156].	142

LIST OF FIGURES

		Page
Figure 2.1	Energy band diagram for a) intrinsic, b) n-type and c) p-type silicon [25,26]	12
Figure 2.2	(a) Plane view and (b) Cross-sectional views of SEM of PS samples (S1, S2, S3) at different current density, (c) Histograms showing particle size and (d) interpore distance distribution of PS samples [37].	16
Figure 2.3	Morphology of FESEM on PS with randomly distributed four-branch-shaped pores, a) 20, b) 40, and c) 60 minutes, leads to the formation of highly connected four-branch-shaped pores [39].	17
Figure 2.4	Morphology of FESEM on PS with different etching time randomly distributed on the surface of the PS, and some pores had star-like appearances and elongated shapes. The pores were increased with the increasing etching time, a) 5, b) 10, c) 15, d) 20, e) 25, and, f) 30 minutes [40].	18
Figure 2.5	XRD pattern analysis of PS and crystalline Si, $2\theta = 33.3^\circ$ correspond to the position of PS and $2\theta = 69.2^\circ$ correspond to the bare crystalline silicon [41].	19
Figure 2.6	Schematic representation of the indirect absorption process in semiconductors, an indirect transition, the indirect transition takes an electron from state 1 into state 2 through a two-step process, involving a virtual optical transition at $k = (0, 0, 0)$ and a phonon scattering of the electron from $k = (0, 0, 0)$ (state 2) to $k = (1, 0, 0)$ (state 3). The final energy of the transition is E_g [44].	21
Figure 2.7	Schematic diagram of reflectance mechanism, which shows a reflection of light from the two interfaces in a PS sample, interference occurs between the reflected beams from the upper and the lower interfaces [43].	21

Figure 2.8	Reflection Spectra of the c-Si compared with the PS Samples (left) and the extrapolation of a straight line using Kubelka-Munk relation for indirect allowed transition of the samples with different etching current densities A) 10 mA/cm ² , B) 20 mA/cm ² , and C) 30 mA/cm ² (right) [46].	22
Figure 2.9	ZnO crystal structures, the small and big dot represent O and Zn atom, (a) cubic rock salt (B1), (b) cubic zinc blende (B3) and (c) hexagonal wurtzite (B4) [55].	24
Figure 2.10	a) Crystal structure of ZnO [57], where the structure of ZnO can simply be described as follows b) countless closely packing O ²⁻ and Zn ²⁺ layers alternately stacked in the direction of the c-axis, with the adjacent layers of O ²⁻ and Zn ²⁺ forming a tetrahedral structure [58].	25
Figure 2.11	LDA band structure of the ZnO crystal, the conduction band minima, and valence band maxima represent ZnO is a direct bandgap semiconductor [61,62].	26
Figure 2.12	UV-Visible reflectance spectra (left) and the extrapolation of a straight line to $(\alpha h\nu)^{1/2} = 0$ gives the value of energy band gap from reflectance spectra, direct transition between valence and conduction bands are a) 3.43 eV and 3.47 eV for ZnO nanorods and nanotubes (right) [62].	27
Figure 2.13	Random distribution of PS and after the growth of ZnO on PS using CBD, a) PS, b) low magnifications, and c) high magnifications of the fabricated ZnO nanofilms surface morphology grown on the PS substrate [65].	29
Figure 2.14	XRD pattern of ZnO nanofilms grown on PS substrate [65].	31
Figure 2.15	XRD analysis of the ZnO on PS layers [69].	32
Figure 2.16	XRD spectra of as-deposited and annealed of ZnO on PS composite films [70].	32
Figure 2.17	Raman scattering analysis of ZnO nanorods grown on PS substrates by VS, at different growth temperatures [39].	33

Figure 2.18	<i>I-V</i> characteristics of the PS substrate and ZnO nanofilms [65].	33
Figure 2.19	Tauc's plots from the samples annealed between (400 to 800) °C. Absorption coefficient was calculated from the reflectance spectra using the Kubelka-Munk relation [71].	34
Figure 2.20	<i>I-V</i> characteristics curves of ZnO/PS under various UV illumination [12].	39
Figure 2.21	Log <i>I-V</i> characteristics of the ZnO nanorods and ZnO seed layer photodetectors measured in dark and under UV illumination [85].	40
Figure 2.22	<i>I-V</i> characteristics of PS MSM photodetector prepared under dark and illumination conditions at 30 mA/cm ² [87].	40
Figure 3.1	Flow chart of all the methodologies in this work.	43
Figure 3.2	Silicon wafer, a) Industry manufactured of n-type silicon doped phosphorus with the orientation of (100), b) The whole substrate place on the diamond cutter, and c) substrates after the cutting process, (12.25 x 12.25) mm.	44
Figure 3.3	a) Materials compartment need for etching and b) experimental set-up connection of materials during electrochemical etching process.	47
Figure 3.4	Electrochemical etching set-up using, a) Keithley 220 Programmable Current Source and 60 W illuminated on the front surface, and b) schematic diagram of the etching technique.	47
Figure 3.5	a) Power supply used during electrochemical etching process (Keithley220 Programmable current source) for the formation of PS, and b) PS substrate produced after etching.	48
Figure 3.6	a) RF sputtering machine (Auto HHV 500 Sputter Coater), and b) schematic diagram of standard operational procedure of RF system.	50

Figure 3.7	The furnace (Naber-Labotherm R70/9) for annealing process.	52
Figure 3.8	a) The raw materials for CBD, Hexamethylenetetramine (left), and Zinc Nitrate Hexahydrate (right), and b) the substrates were placed inclinedly in a beaker during CBD process to achieve a high surface to the volume ratio of ZnO deposited on PS substrate.	54
Figure 3.9	a) Schematic diagram of standard operating procedures of the thermal evaporator and b) dimension of finger mask used for MSM photodetector application.	56
Figure 3.10	a) FESEM machine (FEI Nova NanoSEM 450 FESEM) system, and b) schematic diagram of standard operating procedures for FESEM.	58
Figure 3.11	Schematic diagram of standard operating of EDX.	59
Figure 3.12	Raman Spectroscopy using a) LabRAM HR800 (Horiba Jobin Yvon) Raman spectrometer, and b) schematic diagram of standard operating procedures of Raman Spectrometer.	61
Figure 3.13	The Bragg's law reflection to explain the interference pattern of X-rays scattered by crystals as discussed in equation (3-2).	62
Figure 3.14	The schematic diagram of standard operating procedures of XRD (PANalytical X'pert PRO MRD PW3040).	63
Figure 3.15	a) AFM system (Dimension Edge Bruker AFM), and b) schematic diagram of standard operating procedures of AFM.	67
Figure 3.16	UV-Vis spectroscopy using, a) Cary 5000 UV-Vis-NIR spectrophotometer, and b) Schematic diagram of standard operating procedures of UV-Vis Spectrophotometer for reflection and absorbance.	68
Figure 3.17	Schematic diagram of standard operating procedures of <i>I-V</i> measurement system using Keithley 2400 Series SourceMeters.	70

Figure 3.18	Structure of MSM photodetector using metal contact (Ni) as prepared by this work.	72
Figure 4.1	The weight loss of PS under different etching time of (5, 10, 15, and 20) minutes at constant current flow of 25 mA and using solution of HF and ethanol in ratio of 1:4	76
Figure 4.2	The morphology of FESEM of PS1, PS2, PS3, and PS4 with different etching time of (5, 10, 15, and 20) minutes at constant current flow of 25 mA, using solution of HF and ethanol in ratio of 1:4.	79
Figure 4.3	The AFM analysis of PS1, PS2, PS3, and PS4 with different etching time of (5, 10, 15, and 20) minutes at constant current flow of 25 mA and using solution of HF and ethanol in ratio of 1:4.	80
Figure 4.4	XRD analysis of PS1, PS2, PS3 and PS4 with different etching time of (5, 10, 15, and 20) minutes at constant current flow of 25 mA and using solution of HF and ethanol in ratio of 1:4.	81
Figure 4.5	Raman analysis of PS1, PS2, PS3 and PS4 with different etching time of (5, 10, 15, and 20) minutes at constant current flow of 25 mA and using solution of HF and ethanol in ratio of 1:4.	84
Figure 4.6	UV-Vis diffuse reflectance spectra (left) and the extrapolation of a straight line using Tauc's plot, where α is calculated using Kubelka-Munk relation, $[h\nu \ln [(R_{\max} - R_{\min}) / (R - R_{\min})]^{1/2}$ vs E_g for PS1, PS2, PS3 and PS4 with different etching time of (5, 10, 15, and 20) minutes at constant current flow of 25 mA and using solution of HF and ethanol in ratio of 1:4.	86
Figure 4.7	Percentage of absorption spectra vs wavelength (nm) for PS1, PS2, PS3, and PS4 at different etching time of (5, 10, 15, and 20) minutes at constant current flow of 25 mA and using solution of HF and ethanol in ratio of 1:4.	88
Figure 4.8	The graph of weight loss under different current of (10, 15, 20, and 25) mA at constant etching time of 15 minutes and using solution of HF and ethanol in ratio of 1:4.	90

Figure 4.9	The morphology FESEM of porous silicon PS5, PS6, PS7, and PS8 with different current of (10, 15, 20, and 25) mA at constant etching time of 15 minutes and using solution of HF and ethanol in ratio of 1:4.	92
Figure 4.10	The AFM analysis of PS5, PS6, PS7, and PS8 with different current of (10, 15, 20, and 25) mA at constant etching time of 15 minutes and using solution of HF and ethanol in ratio of 1:4.	94
Figure 4.11	XRD analysis of PS5, PS6, PS7, and PS8 with different current of (10, 15, 20, and 25) mA at constant etching time of 15 minutes and using solution of HF and ethanol in ratio of 1:4.	95
Figure 4.12	Raman analysis of PS5, PS6, PS7, and PS8 using different current of (10, 15, 20, and 25) mA at constant etching time of 15 minutes and using solution of HF and ethanol in ratio of 1:4.	97
Figure 4.13	UV-Visible reflectance spectra (left) and the extrapolation of a straight line of Tauc's plot, where α is calculated using Kubelka-Munk relation, $[hv \ln [(R_{\max} - R_{\min}) / (R - R_{\min})]^{1/2}]$ vs E_g for PS5, PS6, PS7 and PS8 with different current of (10, 15, 20 and 25) mA at constant etching time of 15 minutes and using solution of HF and ethanol in ratio of 1:4.	99
Figure 4.14	Percentage of absorption spectra vs wavelength (nm) for PS5, PS6, PS7, and PS8 using different current of (10, 15, 20, and 25) mA at constant etching time of 15 minutes and using solution of HF and ethanol in ratio of 1:4.	100
Figure 4.15	The morphology FESEM of different thickness of the ZnO _{seed layer} /PS, a) thickness ZnO seed layer of 50 nm, b) thickness ZnO seed layer of 100 nm and c) thickness ZnO seed layer of 200 nm.	102
Figure 4.16	Raman analysis of different thickness of the ZnO _{seed layer} /PS, a) thickness ZnO seed layer of 50 nm, b) thickness ZnO seed layer of 100 nm and c) thickness ZnO seed layer of 200 nm.	103

Figure 4.17	UV-Visible reflectance spectra (left) and the extrapolation of a straight line using Kubelka-Munk plot of optical energy band gap $[h\nu \ln [(R_{\max} - R_{\min}) / (R - R_{\min})]^2$ vs E_g of the different thickness of the $ZnO_{\text{seed layer}}/PS$, a) thickness ZnO seed layer of 50 nm, b) thickness ZnO seed layer of 100 nm and c) thickness ZnO seed layer of 200 nm.	105
Figure 4.18	Percentage of absorption spectra (a.u) vs wavelength (nm) for different thickness of the $ZnO_{\text{seed layer}}/PS$, a) thickness ZnO seed layer of 50 nm, b) thickness ZnO seed layer of 100 nm and c) thickness ZnO seed layer of 200 nm.	106
Figure 4.19	The morphology FESEM of the $ZnO_{\text{CBD}}/ZnO_{\text{seed layer}}/PS$ using seed layer thickness of 50 nm, with increasing CBD growth durations for (1, 3 and 5) hours, (a1, a2, and a3).	109
Figure 4.20	The morphology FESEM of the $ZnO_{\text{CBD}}/ZnO_{\text{seed layer}}/PS$ using seed layer thickness of 100 nm, with increasing CBD growth durations for (1, 3 and 5) hours, (b1, b2, and b3).	110
Figure 4.21	The morphology FESEM of the $ZnO_{\text{CBD}}/ZnO_{\text{seed layer}}/PS$ using seed layer thickness of 200 nm, with increasing CBD growth durations for (1, 3 and 5) hours, (c1, c2, and c3).	111
Figure 4.22	XRD analysis of the $ZnO_{\text{CBD}}/ZnO_{\text{seed layer}}/PS$ using seed layer thickness of 50 nm, with increasing CBD growth durations for (1, 3 and 5) hours, (a1, a2, and a3).	114
Figure 4.23	XRD analysis of the $ZnO_{\text{CBD}}/ZnO_{\text{seed layer}}/PS$ using seed layer thickness of 100 nm, with increasing CBD growth durations for (1, 3 and 5) hours, (b1, b2, and b3).	114
Figure 4.24	XRD analysis of the $ZnO_{\text{CBD}}/ZnO_{\text{seed layer}}/PS$ using seed layer thickness of 200 nm, with increasing CBD growth durations for (1, 3 and 5) hours, (c1, c2, and c3).	115
Figure 4.25	Raman analysis of the $ZnO_{\text{CBD}}/ZnO_{\text{seed layer}}/PS$ using seed layer thickness of 50 nm, with increasing CBD growth durations for (1, 3 and 5) hours, (a1, a2, and a3).	118

Figure 4.26	Raman analysis of the ZnO _{CBD} /ZnO _{seed layer} /PS using seed layer thickness of 100 nm, with increasing CBD growth durations for (1, 3 and 5) hours, (b1, b2, and b3).	118
Figure 4.27	Raman analysis of the ZnO _{CBD} /ZnO _{seed layer} /PS using seed layer thickness of 200 nm, with increasing CBD growth durations for (1, 3 and 5) hours, (c1, c2, and c3).	119
Figure 4.28	UV-Visible reflectance spectra (left) and the extrapolation of a straight line using Kubelka-Munk plot of optical energy band gap, $[h\nu \ln [(R_{\max} - R_{\min}) / (R - R_{\min})]]^2$ vs E_g of the ZnO _{CBD} /ZnO _{seed layer} /PS, using the seed layer thickness of 50 nm, with increasing CBD growth durations for (1, 3 and 5) hours, (a1, a2, and a3).	121
Figure 4.29	UV-Visible reflectance spectra (left) and the extrapolation of a straight line using Kubelka-Munk plot of optical energy band gap, $[h\nu \ln [(R_{\max} - R_{\min}) / (R - R_{\min})]]^2$ vs E_g of the ZnO _{CBD} /ZnO _{seed layer} /PS, using the seed layer thickness of 100 nm, with increasing CBD growth durations for (1, 3 and 5) hours, (b1, b2, and b3).	122
Figure 4.30	UV-Visible reflectance spectra (left) and the extrapolation of a straight line using Kubelka-Munk plot of optical energy band gap, $[h\nu \ln [(R_{\max} - R_{\min}) / (R - R_{\min})]]^2$ vs E_g of the ZnO _{CBD} /ZnO _{seed layer} /PS, using the seed layer thickness of 200 nm, with increasing CBD growth durations for (1, 3 and 5) hours, (c1, c2, and c3).	123
Figure 4.31	Percentage of absorption spectra vs wavelength (nm) of the ZnO _{CBD} /ZnO _{seed layer} /PS using the seed layer thickness of 50 nm, with increasing CBD growth durations for (1, 3 and 5) hours, (a1, a2, and a3).	125
Figure 4.32	Percentage of absorption spectra vs wavelength (nm) of the ZnO _{CBD} /ZnO _{seed layer} /PS using the seed layer thickness of 100 nm, with increasing CBD growth durations for (1, 3 and 5) hours, (b1, b2, and b3).	125
Figure 4.33	Percentage of absorption spectra vs wavelength (nm) of the ZnO _{CBD} /ZnO _{seed layer} /PS using the seed layer thickness of 200 nm, with increasing CBD growth durations for (1, 3 and 5) hours, (c1, c2, and c3).	126

Figure 4.34	<i>I-V</i> measurements on MSM PDs of a) Ni/PS/Ni, and b) annealed-(Ni/PS/Ni).	129
Figure 4.35	<i>I-V</i> measurements on MSM PD of a) Ni/ZnO/PS/Ni, and b) annealed-(Ni/ZnO/PS/Ni).	131
Figure 4.36	Responsivity as a function of wavelength at a bias of +5V for MSM PD, a) Ni/PS/Ni and b) annealed-(Ni/PS/Ni).	133
Figure 4.37	Responsivity as a function of wavelength at a bias of +5V for MSM PD, a) Ni/ZnO/PS/Ni and b) annealed-(Ni/ZnO/PS/Ni).	135
Figure 4.38	Photocurrent sensitivity measured at a bias of +5 V with illumination turned on and off repeatedly for fabricated MSM PD, a) Ni/PS/Ni and b) annealed-(Ni/PS/Ni).	137
Figure 4.39	Photocurrent sensitivity measured at a bias of +5 V with illumination turned on and off repeatedly for fabricated MSM PD, a) Ni/ZnO/PS/Ni, and b) annealed-(Ni/ZnO/PS/Ni).	138
Figure 4.40	Sensitivity as a function of time at a bias of +5 V with UV and visible illumination turned on and off at constant durations, a) Ni/PS/Ni, and b) annealed-(Ni/PS/Ni).	140
Figure 4.41	Sensitivity as a function of time at a bias of +5 V with UV and visible illumination turned on and off at constant durations, a) Ni/ZnO/PS/Ni, and b) annealed-(Ni/ZnO/PS/Ni).	141

LIST OF SYMBOLS

A	Area
A	Illuminated Area
\AA	Angstrom
a, b, c	Lattice constant
a.u	Arbitrary unit
c_0	Lattice constant in c -axis for bulk material
D	Crystallite size
E_F	Fermi level
E_g	Energy Band gap
$e-h$	Electron-hole
eV	Electron volt
E_V	Valance band energy level
ϵ_c	Strain
h	Plank's Constant
hkl	Miller indices
I	Intensity of the transmission light
I_{dark}	Dark Current
I_L	Current under Light
I_o	Intensity of the incident light
I_{ph}	Photocurrent
I-t	Current-Time
$I-V$	Current-Voltage
m	Mass

$^{\circ}\text{C}$	Celsius degree temperature
P	Power of the light
P_{in}	Incident Optical Power
ϕ_s	Semiconductor work function
R	Responsivity
S	Sensitivity
T	Temperature
ν	Frequency
α	Absorption Coefficient
θ	Bragg's angle
λ	Wavelength
ν	Light frequency
Φ	Work function

LIST OF ABBREVIATIONS

AFM	Atomic Force Microscopy
Ar	Argon
AR	Anti-reflection
CB	Conduction Band
CBD	Chemical Bath Deposition
CXA	Computer X-ray Analyzer
CZ	Czochralski
DC	Direct Current
DI	Deionized water
EDX	Energy-Dispersive X-ray
FESEM	Field Emission Scanning Electron Microscopy
FET	Field-effect Transistors
HF	Hydrofluoric acid
ICDD	International Centre for Diffraction Data
IUPAC	International Union of Pure and Applied Chemistry
IV	Current–Voltage
LED	Light Emitting Diodes
MBE	Molecular Beam Epitaxy
MOCVD	Metal-Organic Chemical Vapour Deposition
MSM	Metal-Semiconductor-Metal
NOR	Nano-Optoelectronics Research and Technology
OPS	Oxidized Porous Silicon
PL	Photoluminescence

PS	Porous Silicon
PVD	Physical Vapor Deposition
RF	Radio Frequency
SEM	Scanning Electron Microscopy
Si	Silicon
SiO ₂	Silicon dioxide
SRO	Silicon-rich-oxide
UV	Ultraviolet
UV-Vis	Ultraviolet–visible
VB	Valence Band
VS	Vapor Solid
XRD	X-Ray Diffraction
ZnO	Zinc Oxide

PENCIRIAN SILIKON BERLIANG DAN ZINK OKSIDA/SILIKON BERLIANG UNTUK APLIKASI PENGESAN FOTO

ABSTRAK

Zink Oksida (ZnO) digunakan secara meluas bagi pembangunan peranti optoelektronik dan elektronik seperti pengesan foto, piezoelektrik, transistor kesan medan (FET), diod pemancar cahaya (LED), fotovolta, pengesan kimia dan lain-lain kerana mempunyai kemampuan tindak balas yang cepat, gandaan optik yang tinggi, nisbah permukaan ke isipadu yang tinggi, dan mempunyai orientasi kristal tertentu. Sementara itu, silikon berliang (PS) telah menarik banyak perhatian kerana aplikasinya dalam pembangunan peranti optoelektronik berasaskan silikon disebabkan kebolehlaraan kekasaran permukaan, dan keupayaannya untuk mengurangkan ketidakpadanan pemalar kekisi dengan pembentukan lapisan berliang. Menggabungkan kedua-dua bahan, kajian dilakukan untuk mensintesis dan mencirikan sifat-sifat pertumbuhan ZnO pada PS. Substrat PS telah disediakan dengan menggunakan perubahan kadar masa penghakisan dan arus. Didapati bahawa kadar punaran adalah pada arus 25 mA dan masa punaran selama 15 minit di atas permukaan Si jenis n yang berorientasikan (100) dapat mencapai permukaan liang seragam dan sifat optik yang baik. Kemudian, ZnO dipercikan ke substrat PS oleh percikan frekuensi radio untuk lapisan benih. Lapisan benih membantu pemusatan ZnO dan menggalakkan perkembangan penumbuhan struktur hablur ZnO menerusi arah satah kekisi c. Ketebalan lapisan yang berbeza pada (50, 150, dan 200) nm telah dipercikan. Kemudian, penumbuhan struktur ZnO menggunakan teknik pemendapan rendaman kimia (CBD) dengan masa pertumbuhan yang berbeza (1, 3 dan 5) jam. Analisis

morfologi menunjukkan bahawa mikrostruktur ZnO telah tumbuh secara rawak pada dan dalam struktur PS. Dengan peningkatan jumlah lapisan benih dan masa pertumbuhan, lebih tinggi jumlah peratusan atom dan peratusan berat oksigen dan zink. Spektrum belauan sinar-X (XRD) menunjukkan pertumbuhan ZnO yang berkualiti tinggi dalam satah (100), (101) dan (002). Analisis serakan Raman menunjukkan peralihan puncak E₂ (Tinggi), mencirikan kekisi wurtzite dan menunjukkan kehabluran ZnO yang baik. Untuk menguji keupayaan sampel ini sebagai peranti, pengesan foto Logam-Semikonduktor-Logam, (MSM) di reka menggunakan logam Ni dan dibentuk pada sampel. Parameter bagi penubuhan sampel adalah seperti berikut. Silikon berliang terbentuk dengan masa punaran selama 15 minit dan arus 25 mA. Untuk sampel ZnO, ketebalan benih adalah 200 nm dan masa pertumbuhan CBD selama 5 jam. Sentuhan Schottky yang baik dan tindak balas foto yang pantas telah ditunjukkan oleh pengesan foto ujian Logam-Semikonduktor-Logam yang telah disempuh lindap.

CHARACTERIZATION OF POROUS SILICON AND ZINC OXIDE/POROUS SILICON FOR PHOTODETECTOR APPLICATION

ABSTRACT

Zinc Oxide (ZnO) is widely used for the development of optoelectronic and electronic devices such as photodetectors, piezoelectric, field-effect transistors (FET), light emitting diodes (LED), photovoltaic, chemical sensors and others, because of its capability of fast response, high optical gain, high surface-to-volume ratio, and specific crystalline orientation. Meanwhile, porous silicon (PS) has drawn much attention for its application in the development of silicon-based optoelectronic devices due to its adjustable surface roughness and its ability to reduce the large mismatch in the lattice constants with the formation of porous layer. Merging both materials, the work is carried out to synthesize and characterize the properties of ZnO growth on PS. The PS substrates were prepared by using different parameter of etching time and current. It was found that, the etching condition is at current of 25 mA and 15 minutes etching time on *n*-type Si substrate with orientation (100) would achieve a uniform porous surface and good optical properties. Later, ZnO was sputtered onto the PS substrate by RF as a seed layer. The seed layer assists the nucleation of ZnO also promotes the growth development of ZnO wurtzite crystal structure along *c*-axis orientation. The different seed layer thickness of (50, 100, and 200) nm were sputtered. Then, the growth of ZnO structure was performed using chemical bath deposition (CBD) technique with different growth time of (1, 3 and 5) hours. Morphological analysis show that the grown ZnO microstructures covered randomly on and into the PS structure. With the increase in the amount of seed layer and the growth time, the higher

distribution for atomic and the weight percentage of oxygen and zinc. The X-ray diffraction (XRD) spectra indicate a high-quality growth of ZnO in lattice direction of (100), (101) and (002). Raman scattering analysis revealed the peaks shift of E_2 (High), characterized a wurtzite lattice and indicates a good crystallinity of the ZnO. To test the performance as a device, an MSM photodetectors (PDs) were fabricated with Ni contact formed on the samples. The growth parameter of the samples are set as follows. PS is formed at the etching time of 15 minutes and current of 25 mA. For ZnO, the thickness of seed layer is 200 nm, and CBD growth time of 5 hours. A good Schottky contact and photo-responsivity has been demonstrated from the annealed MSM PDs test device.

CHAPTER 1 - INTRODUCTION

1.1 Introduction

This chapter clarify the background, problem statement, research objective, research hypothesis, scope of the study, and thesis organization by chapter of this work on the title of “Characterization of Porous Silicon and Zinc Oxide/Porous Silicon for Photodetector Application”. Some of the ideas were inspired from literature review of other works.

1.2 Background

Zinc oxide (ZnO) is a II-VI compound semiconductor. ZnO has a wide band gap of 3.37 eV and large exciton binding energy of 60 meV, allows for excitonic transitions even at room temperature and high radiative recombination efficiency for spontaneous emission [1]. ZnO is intrinsically *n*-type semiconductor, partly due to natural doping by interstitial Zn atom or oxygen vacancy and naturally crystallizes in the hexagonal wurtzite structure [2]. ZnO has potential in the development of optoelectronic and electronic devices such as photodetectors, piezoelectronics, field effect transistors, light emitting diodes, chemical sensors, photovoltaic devices [3] and others because of its capability of fast response, high optical gain, high surface-to-volume ratio, and specific crystalline orientation. ZnO has its own intrinsic defects cause by the oxygen vacancies and/or zinc interstitials. ZnO plays a vital role in UV detection mechanism and the ZnO is extremely conductive and sensitive to UV light exposure [4].

PS has large internal adjustable roughness [5], and strong absorbability properties [6]. Moreover, PS prepared by the silicon provides a possibility to integrate PS-based optical devices [7]. PS is important Si-based materials because its open structure and large surface area, combined with its unique optical and electrical properties as a template [8]. PS layer can reduce the large mismatches in the lattice constants between the ZnO and Si substrates [10,11] as formation of PS can decrease the lattice constants of Si. Lately, PS used as a good growth template for epitaxial re-growth due to reduce the density of structural defects intentionally and allows the growth of residual free epitaxial ZnO layers [10].

Fabrication of MSM PDs requires the interface of metal-semiconductor having a large Schottky barrier height, leads to a small leakage current and high breakdown voltage. MSM PD, the thermal treatment is important due to enhance the photoresponsivity [11]. This converts the responsiveness in terms of photocurrent to dark current ratio [11].

1.3 Problem statement

There is numerous of works study the PS surface on *c*-Si as a base substrate and the incorporation of ZnO on the PS structure. R. Shabannia works on the PS with small pores size acts as a base substrate, then grow the ZnO by seed layer and CBD method, ZnO nanorod arrays were well aligned, compact, and perpendicular to the PS substrate, thus the fabrication of MSM PDs just focussed on the sensitivity of ZnO layer, the maximum responsivity was 1.736 A/W at +1 V bias voltage under a 325 nm illumination [12]. Other than that, there are also a lot of works focused on the synthesized of ZnO on the different substrate such as ZnO MSM UV PDs on glass, the maximum responsivity is 0.19 A/W under illumination of 365 nm [13], and ZnO MSM UV PDs on PPC plastic with various metal contacts, the responsivity values are 0.082 A/W using Pd, 0.098 A/W using Ni and 0.116 A/W using Pt by 365 nm [14]. There are also some works focused on the ability of PS as MSM PDs. B. E. Batool claimed that the n-type Si (100) substrates, fabrication of macroporous structure, the responsivity recorded is 0.17A/W (Pt/PS/Pt) under 530 nm and the relatively weaker peak at 765 nm emerged from PS/Si junction [11]. Other than that, M. Zerdali work on n-type, small pore size, the MSM PD was fabricated by Ni contact, (Ni/PSi/*c*-Si/Ni) and achieved the photocurrent is maximum responsivity at the wavelength of 546 nm [15]. Normally, ZnO detector is irradiated by UV light with energy higher than the bandgap (3.37 eV for ZnO), ehp will be generated, as a result these excess charge carriers contribute to photo current and result in the response to the UV light [14] while PS mostly response in visible light [15].

This work claimed that the growth of ZnO was deposited in and on the PS surface as the pores on *c*-Si surface are bigger and focussed on the incorporation between

them. This work used the PS structure with macropore size as a base substrate to apply its potential in applications as photodetection. The unique performance of the incorporation of ZnO structure on macroporous *c*-Si substrate as potential applications in photodetection was studied. There is no other work that apply the potential on this structure and capability as an MSM PDs on the growth of ZnO structure on the macroporous size of the PS layer, most of them elaborate the performance of UV PDs by performance of synthesized ZnO as the nanorods produced were vertically aligned, dense on the surface, and perpendicular to the PS substrate. In this work, the photodetection giving two spectra signal (UV and Vis) which higher in visible compared to UV range comes from both structure's sensitivity which are ZnO and macroporous *c*-Si. The ZnO has a potential application in the UV detection while the PS has high sensitivity in visible detection application. The MSM structure was fabricated because it has very fast photon response and low cost of fabrication. In this work, the performance of ZnO structure on PS substrate as MSM photodetector will be discussed.

1.4 Research Objectives

The objectives of this project:

1. To study the physical properties of PS as a base substrate.
2. To study the incorporation of ZnO in the PS structure.
3. To investigate the performance of ZnO structure on PS substrate as potential applications in photodetection.

1.5 Research Hypothesis

1. PS contains following research hypothesis:
 - The morphology of PS on n-type Si (100) leads to formation of four-branch-shape pores arrangement (PS) and macroporous PS will aligned on a silicon substrate using of HF and ethanol in ratio of 1:4.
 - The higher the etching time and current density, increase distribution of pores and more percentage of atomic and weight of oxide element compare while decreasing the percentage of Si.
2. The growth and characterization of ZnO on PS has following research hypothesis:
 - Thin film of ZnO deposited onto a PS substrate has served as a seed layer not only to facilitate the nucleation of ZnO but also to decrease the lattice mismatch between them. As the seed layer thickness thicker, the seed layer deposited much and the growth of ZnO will align on and into the PS substrate.

- Investigation of the different growth time of synthesizes ZnO microstructures on and into PS substrate by CBD method. Randomly oriented growth of ZnO on and into PS surface, as PS surface is exhibited like amorphous surface and multicrystalline silicon substrate.
3. Potential as an MSM PDs has following research hypothesis:
- Schottky contact of MSM PD, having a good signal of photocurrent, responsivity, and photoresponse as correspond to ZnO layer sensitive to UV and PS layer sensitive to visible range.
 - The thermal treatment (annealed) to the contact attributed to the rising of Fermi level into the conduction band which leads to widening optical band gap also attributed to better Schottky contact.

1.6 Scope of The Study

Based on the objectives, the scopes of the study are projected as following:

- Characterization of PS morphology and structural properties.
- PS layer produced based on the uniformity PS morphological and has good structural also optical properties act as a base substrate.
- Characterization of different seed layer thickness, morphology and structural using FESEM, UV-Vis and Raman spectroscopy.
- Synthesis of ZnO on PS substrates under different growth duration conditions using CBD technique on the different seed layer thickness on the optimized PS surface.
- Optical characterization via UV-Vis absorption, structural and morphology characterization using XRD, FESEM, and Raman spectroscopy.
- Fabrication of the MSM PD using Ni contact.

1.7 Thesis Organization

Thesis organization is prepared by chapter, based on following:

Chapter 1 briefing the introduction, problem statement, research objective, research hypothesis, scope of the study, and thesis organization by chapter of this work.

Chapter 2 provides literature reviews such as the basic properties, background, growth mechanism, structural properties, and optical properties from books, papers and journals of PS, ZnO, the incorporation between them and MSM PD which related to this work.

Chapter 3 describes the equipment used for sample preparation, working principle, and different methods of characterization. The basic principle of FESEM, EDX, XRD, AFM, Raman Spectroscopy, UV-Vis Spectroscopy and *I-V* measurement also will be explained.

Chapter 4 focusses on the analysis of the data, explanations of graph and analysis result gained from the characterization. The morphology, structural, optical and electronic properties are discussed for PS, the growth of ZnO microstructures on PS and also the discussion for the performance of MSM PD.

Chapter 5 represents the conclusion of this work and future work. The conclusion will summarize all the result. Future work will be giving many new notions depending on the several studies that can be suggested.

CHAPTER 2 - LITERATURE REVIEW

2.1 Introduction

In this chapter, the basic properties, backgrounds, structures of Si and ZnO, also the growth techniques of ZnO using CBD method will be described. In later discussion, the ability of ZnO on PS as an MSM photodetector also will be reviewed. Most of the work had provided a strong fundamental viewpoint as well as motivation to carry on this research further.

2.2 Introduction to Porous Silicon

A great number of works had reported the interest on PS structure as an attractive material for application in photonics and electronics [16]. PS can be considered as a silicon crystal composed of discontinuous silicon filaments and nano-sized air holes, called pores [17]. PS structure is usually designed by anodic electrochemical etching of silicon wafer. The pore formation mechanism requires electronic holes for facilitating dissolution reactions. The external illumination of the n-type substrate is required, to reach holes concentrations for pore formation. It is obtained by the electrochemical dissolution of Si wafers in aqueous hydrofluoric acid (HF) solution or by electrochemical etching in an HF solution containing an oxidizing agent. The darkness and illumination are necessary for *p*-type and *n*-type Si substrates, to realize the etching process. Ethanol is added to the HF electrolyte to respond the hydrophobic character of silicon, facilitate the penetration of HF inside the pores and assist to eliminate the hydrogen bubbles created during pore formation [18].

Nanostructured oxidized PS revealed a wide band gap (E_g) compared to silicon [19]. Silicon-rich-oxide (SRO) or PS had established much interest for its high UV photoconductive properties [20]. Meanwhile, the oxidized porous silicon (OPS) that formed have better sensitivity than its unoxidized counterpart [21].

2.2.1 Basic Properties of Silicon

Silicon belongs to group 14 of the periodic table that also includes C, Ge, Sn, and Pb. The element has an atomic number of 14, and an atomic mass of 28 [22]. Silicon is under metalloids (group IV semiconductor) which means it has combination properties of metals and non-metals and exhibits semi-conducting materials. The group include Boron, Germanium, Arsenic, Antimony, Tellurium, and Polonium. Metalloids share the properties of metals and some non-metallic characteristic. They are normally shiny or dull, usually conduct heat and electricity, ductile, malleable and may gain or lose electrons in reactions. Table 2.1 shows the basic information and properties of silicon [19,21,22].

There are several crystal defects usually incorporated in silicon such as point, line, area and volume defects. The point defect usually occurs because of large or small substitutional impurity, an interstitial silicon atom, and interstitial impurity. The line defect usually caused by edge dislocation. Furthermore, the area and volume defects may cause by surface, voids, and precipitates of the other atoms on silicon [24].

Table 2.1: Basic information and properties of silicon [19,21,22].

Atomic Weight	28.09
Electron configuration	[Si] 3s ² 3p ²
Crystal structure	Diamond
Lattice constant (Angstrom)	5.43095
Density (g/cm ³)	2.328
Density (atoms/cm ³)	4.995 x 10 ²²
Dielectric Constant	11.9
The density of states in the conduction band, N_c (cm ⁻³)	3.22 x 10 ¹⁹
Density of states in valence band, N_v (cm ⁻³)	1.83 x 10 ¹⁹
Electron affinity, X (V)	4.05
Energy gap (eV) at 300K	1.12
Mobility (cm ² / V sec), μ (electrons)	1500
Mobility (cm ² / V sec), μ (holes)	450
Optical-phonon energy (eV)	0.063
Specific heat (J/g °C)	0.7
Thermal conductivity (W/cm °C)	1.5
Thermal diffusivity (cm ² /s)	0.9
Index of refraction	3.42

Figure 2.1 represents the energy band diagram of silicon. The respective doping concentration (cm⁻³), n for electron and p for the hole. For n -type:

$$n = N_c x e^{\left(\frac{E_c - E_F}{kT}\right)} \quad (2-1)$$

For p -type:

$$p = N_v x e^{\left(\frac{E_F - E_v}{kT}\right)} \quad (2-2)$$

where n is a concentration of electron carriers (cm⁻³), p is a concentration of hole carriers (cm⁻³), E_c and E_v are the energy level of the conduction band and valence band, E_F is the Fermi level, N_c and N_v are the intrinsic density of states in conduction and valence band in (cm⁻³).

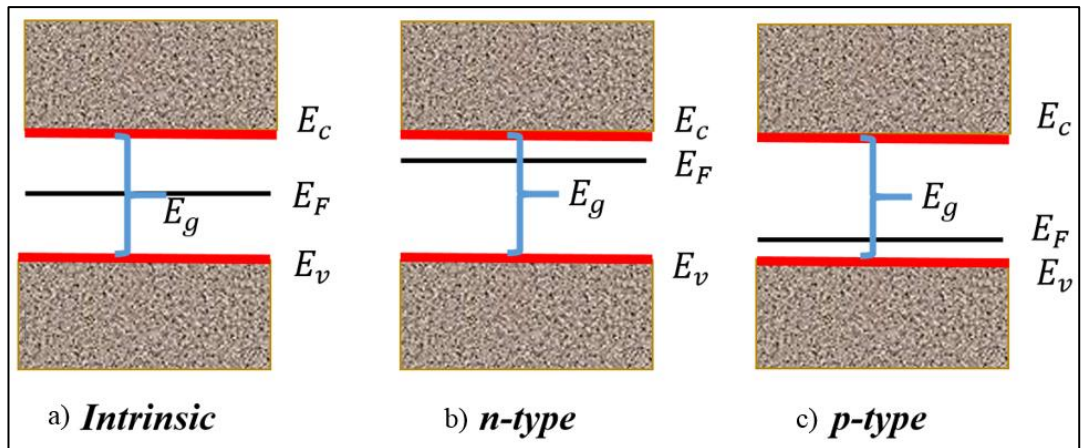


Figure 2.1: Energy band diagram for a) intrinsic, b) *n*-type, and c) *p*-type silicon [25,26].

Silicon wafer is produced by Czochralski (CZ) crystal growth technique. The process is started by electronic grade silicon (EGS), which then melted in the furnace about its melting point at 1412 °C. The Argon is used in the furnace chamber to reduce impurities and the crucible is made of silicon dioxide (SiO_2) to reduce and lowest the contaminant effect. The dopant material (*n*-type or *p*-type) is added to the silicon melt. A seed crystal with desired orientation is dipped in the molten silicon. This seed crystal is rotated and solidify in the equivalent orientation. Then, the ingot with the weighing of nearly 800 kg is produced. The shaping is starting by ground the ingot to have a uniform diameter and remove both ends of the ingot. The cutting process is conducted by industrial-grade diamond-tipped saws to have a symmetrical size [28].

2.2.2 Background of Porous Silicon

Semiconductor developers perceived that electropolishing process of bulk Si left certain rough areas called porous, and they observed these as imperfect areas. PS was accidentally discovered by the Arthur Uhlir Jr. and Ingeborg Uhlir while working at Bell Laboratories in 1950. During this time, they were trying to develop a technique for shaping the surfaces of Si by an electrochemical method, for the application in microelectronic circuits [29]. It was not until Leigh Canham, a scientist with the collaboration of DERA (the UK's Defence Evaluation and Research Agency) in 1990 discover that PS emits visible light when illuminated by UV source. This morphological state of the material later came to attract significant research interest. Moreover, in 1992 researchers revealed that PS can emit light when an electric current is applied, a finding that raised prospects for new optoelectronic sensors and other devices, coupling light to electronics, including future high-speed computers [30].

2.2.3 Structure of Porous Silicon

PS can be characterized from any materials with different pore sizes (millimetre, micrometer, and nanometre), the pores arrangement is ordered or irregular, various type of chemical compositions and using different preparative or electrolyte. There are three pore sizes from the International Union of Pure and Applied Chemistry (IUPAC). The microporous which has pore smaller than 2 nm, mesoporous, the size is between (2 and 50) nm while for macroporous, the pore size larger than 50 nm. The microporous has a high porosity, while mesoporous has a medium porosity and macroporous has a very low porosity as stated in Table 2.2.

Table 2.2: IUPAC recommended the universal of classification of pore size distributions conjunction with electron microscopy data by representing the average percentage of porosity [31].

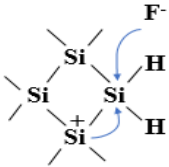
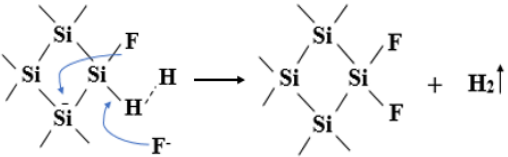
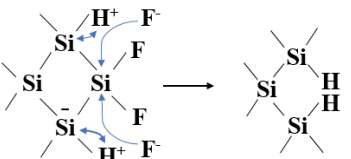
Type	Pore size distribution	Average porosity
Microporous	< 2 nm	80 %
Mesoporous	2 nm < x < 50 nm	30 % - 70 %
Macroporous	> 50 nm	< 10 %

Variability parameters that can affect the porous structure also the distribution of pores include the etching time, current density, type of Si wafer, HF concentration, dopant concentration and temperature. PS can have a different shape of pores depends on the variables such as electrolyte, concentration, current, silicon doping type, density and temperature. It must be noted that the pore walls are amorphous and they are not crystalline [32]. The PS has helped in providing appropriate surfaces or planes for Zn or ZnO seed nucleation at the initial stage so that the subsequent promote the growth of ZnO structures [33]. Furthermore, the skeleton of Si is important for reducing the stress induced at the cooling phase and limiting the formation of dislocation or cracks in ZnO layers [10].

2.2.4 Growth Mechanism of Porous Silicon

The formation of porous structure of *n*-type Si (100) is purely based on the chemical reaction between HF electrolyte on surface of the silicon wafer. The mechanism is based on the capture of holes and electron injection process in four steps, as tabulated in Table 2.3. Step by step formation and growth mechanism due to dissolution chemistry of silicon anodically biased in hydrofluoric acid are shown.

Table 2.3: Description of PS layer formation and growth mechanism due to dissolution chemistry of silicon anodically biased in hydrofluoric acid [34,35].

Description	Mechanism
A hole reaches the surface for a nucleophilic attack on Si-H bonds by F ⁻ from the HF electrolyte (the hole can then migrate on to a Si-H bond), thus releasing a proton.	 <p style="text-align: right;">(2-3)</p>
A second attack is accomplished by another F ⁻ , causing the evolution of molecular H ₂ and electron injection into the substrate. The attack of the Si radical by F ⁻ causes electron injection into the silicon conduction band and the formation of a Si-F bond.	 <p style="text-align: right;">(2-4)</p>
By removal of -SiF ₂ by the replacement of protons in the highly oxidized silicon with the current injection of an electron into the conduction band. A chemical reaction occurs in which HF is added to the one remaining Si-Si bond to release SiF ₄ into solution, and in this step, a tetrafluoride (SiF ₄) molecule is produced.	 <p style="text-align: right;">(2-5)</p>
The tetrafluoride molecule reacts with two HF molecules and H ₂ SiF ₆ is the final product in solution.	$\begin{array}{c} \text{F} & & \text{F} \\ & \diagdown & / \\ & \text{Si} & \\ & / & \diagdown \\ \text{F} & & \text{F} \end{array} \xrightarrow{2\text{HF}} \text{H}_2\text{SiF}_6 \longrightarrow \text{SiF}_6^{2-} + 2\text{H}^+$ <p style="text-align: right;">(2-6)</p>

2.2.5 Structural Properties of Porous Silicon

There are various structural properties of PS layer that form after the etched process depends on the parameters used during electrochemical etching. The shape of individual pores on n-type silicon tend to change from circular to the square to star-like and to dendrite-like with increasing potential [36]. Current density normally affects the pore diameter. Pore diameter increased with increasing the potential and current density. As reported by Martha Ramesh et.al [37], the increase in pore diameter and a decrease in the interpore distance with current density. The oxide layer starts to form at the bottom of pores by increasing current density will increase the coverage of the oxide film and the bottom of the pore will increase ensuing in larger pores and smaller interpore distance, as shown in Figure 2.2.

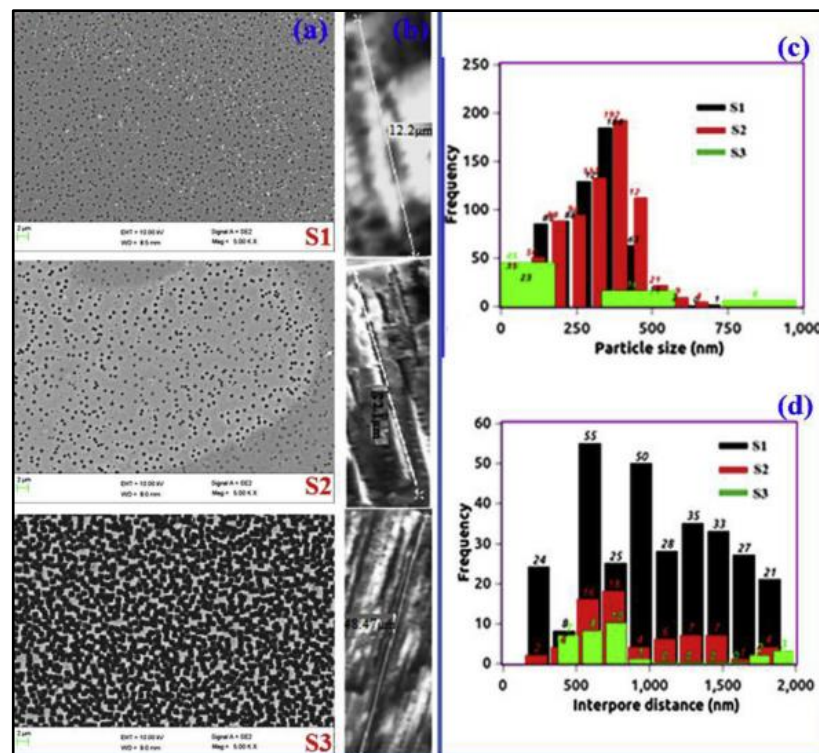


Figure 2.2: (a) Plane view and (b) Cross-sectional views of SEM of PS samples (S1, S2, S3) at different current density, (c) Histograms showing particle size and (d) interpore distance distribution of PS samples [37].

The surface nature of the PS was converted from hydrophilic to hydrophobic when the current density is increased. The figures indicate the sponge-like structure of PS layer with increasing current density, from (30 to 90) mA/cm² with increasing the surface roughness and particle size [38].

Furthermore, etching time for electrochemical etching acts as a primary role in producing porous layer. Nurul Izni proposes *n*-type (100) Si wafer with that etched process using solution of 48 % HF and 95 % ethanol with a volume ratio of 1:4 mostly in the lateral or horizontal directions precisely in the <001> and <010> directions along with vertical or <100> direction [39]. It was stated that etching time is conducted from (20, 40 and 60) minutes leads to the formation of connected four-branch-shaped pores shows by three successive phases. By increasing the etching time, the increase of pore density is detected as shown in Figure 2.3. As the front-side is illuminated, this makes holes continuously generated, thus the number of existing holes is larger than the consumed holes at the tip. Later, these holes are continuously transported in the electric field and attempt to penetrate the porous structure, pore wall and dissolution takes place on the surface of the pore walls. Basically, these holes tend to move to the electrically enhanced places, such as pre-etched initial pits and pore walls formerly known as pore formation sites [39].

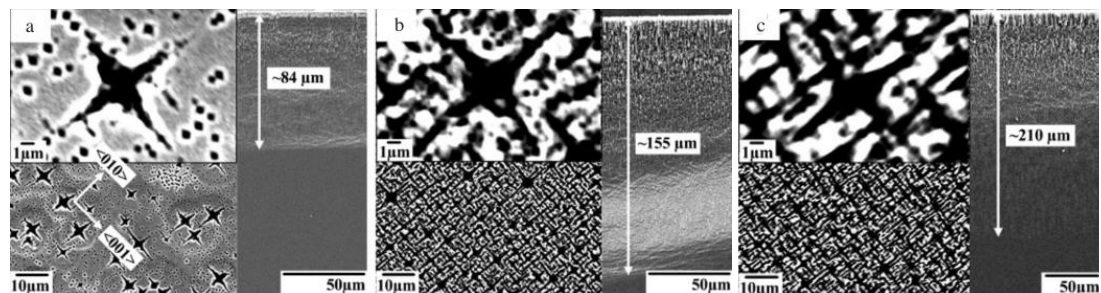


Figure 2.3: Morphology of FESEM on PS with randomly distributed four-branch-shaped pores, a) 20, b) 40, and c) 60 minutes, leads to the formation of highly connected four-branch-shaped pores [39].

Khaldun A. Salman also reported n-type Si wafer (100) orientation as in Figure 2.4, the etching process was done in (5 to 30) minutes using solution of HF and ethanol in ratio of 1:4 to prepare the PS layers. The pores have similar shapes and only the pore diameters were increased, and the pore walls were broadened, directed to the decreased number of pores on the PS surface, later, the porosity was reduced. [40].

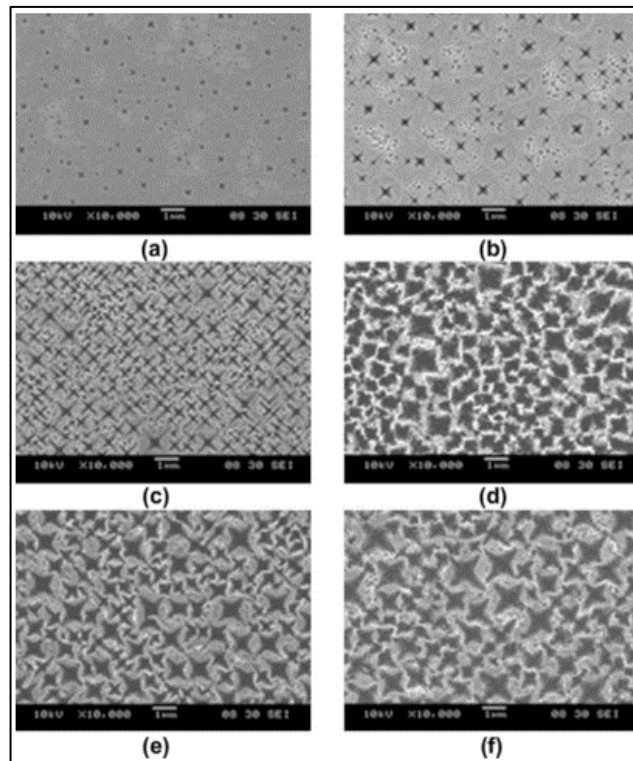


Figure 2.4: Morphology of FESEM on PS with different etching time randomly distributed on the surface of the PS, and some pores had star-like appearances and elongated shapes. The pores were increased with the increasing etching time, a) 5, b) 10, c) 15, d) 20, e) 25, and f) 30 minutes [40].

The XRD analysed the PS and crystalline Si, the peak at $2\theta = 33.3^\circ$ corresponds to formation of PS structures at (211) with little broadening, indicates the crystalline nature of the silicon pores. The peaks at 69.2° correspond to the bare crystalline silicon (c-Si) substrate retain as shown in Figure 2.5 [41].

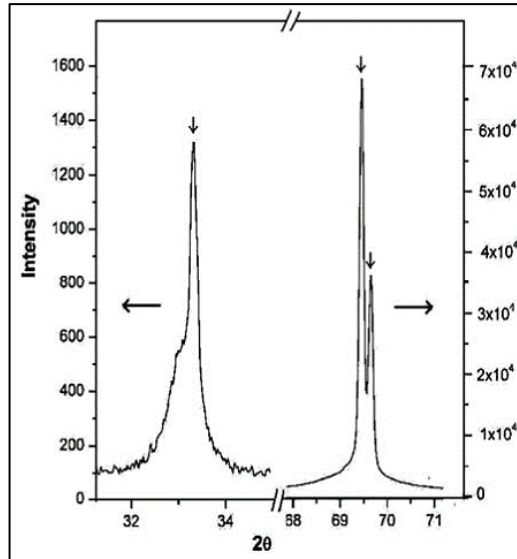


Figure 2.5: XRD pattern analysis of PS and crystalline Si, $2\theta = 33.3^\circ$ correspond to the position of PS and $2\theta = 69.2^\circ$ correspond to the bare crystalline silicon [41].

2.2.6 Optical Properties of Porous Silicon

The etching of the *n*-type PS is difficult because the reaction needs holes to react. To overcome this problem during etching, the sample was illuminated with a 100 W bulb to produce more hole carriers [42]. In a *n*-type, holes are the minority carriers, hence the number are needed to be increased by some external source. The illumination is necessary for pore formation in silicon due to the excess holes present in the material [43]. This property indicates that the *n*-type porous silicon is a better candidate for the application in optoelectronics than the *p*-type porous silicon. As the fact that, the bulk silicon has an indirect band gap of 1.1 eV at room temperature. S. M Prokes and O. J Glembocki et al. mentioned the mechanisms of visible light emission in porous silicon [44]. In crystalline solids, optical transitions must conserve momentum and indirect transitions in *k*-space exploit phonons to conserve the momentum.

A typical indirect absorption process in Si is showing in Figure 2.6. In this case, the absorption process where the virtual optical transition occurs at $k = 0$, from state 1 to state 2 followed by the electron's being scattered in the conduction band by absorbing or emitting a phonon. This takes the photoexcited electron from state 2 at $k = 0$ to state 3, at $k = (100)$. A transition can occur involving a virtual optical transition at $k = (100)$ and a hole scattering from $k = (100)$ to $k = 0$, the final energy of the transition is energy gap, E_g .

PS layer has a rough surface that effective in absorbing more photon than reflected it. By increasing the current density, the reflectance decreases [45]. The schematic diagram of reflectance mechanism shows a reflection of light from the two interfaces in a PS sample. The interference occurs between the reflected beams from the upper and the lower interfaces also constructive interference of the reflected light from the two interfaces. M. Das and D. Sarkar also report that by increasing the current density during the etching process, the value of n is seen to decrease and the porosity is increased from 55 to 78 % [43]. K. A. Salman state that the reflectance was recorded from the PS layer at 5 to 20 min etching time, obviously reduced the light reflection and thus increased the light-trapping at wavelengths ranging from 400 to 1000 nm [40]. Figure 2.7 shows the reflectance mechanism diagram which explains the reflectance on PS layer [43].

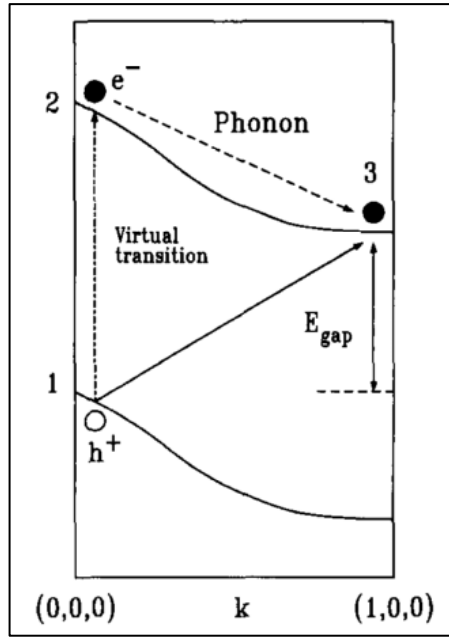


Figure 2.6: Schematic representation of the indirect absorption process in semiconductors, an indirect transition, the indirect transition takes an electron from state 1 into state 2 through a two-step process, involving a virtual optical transition at $k = (0, 0, 0)$ and a phonon scattering of the electron from $k = (0, 0, 0)$ (state 2) to $k = (1, 0, 0)$ (state 3). The final energy of the transition is E_g [44].

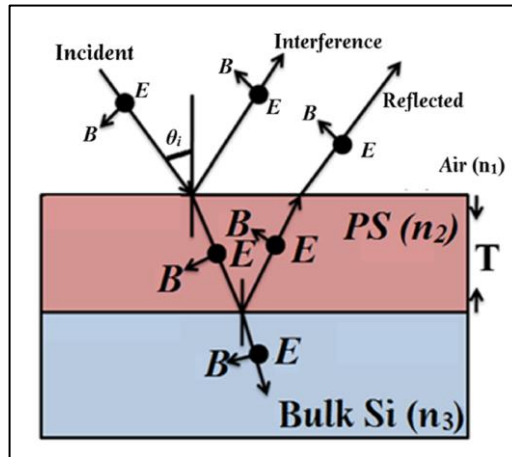


Figure 2.7: Schematic diagram of reflectance mechanism, which shows a reflection of light from the two interfaces in a PS sample, interference occurs between the reflected beams from the upper and the lower interfaces [43].

The optical energy band gap by reflectance spectroscopy can be calculated using Tauc's relation [46]:

$$\alpha hv = A(hv - E_g)^n \quad (1-1)$$

where E_g is the energy gap, hv is the energy of photon, A is a constant and n is an index which $n = \frac{1}{2}$ for allowed direct transition and $n = 2$ for allowed indirect transition of PS. Then, the diffused reflectance measurements are very important for determination of the absorption coefficient, α for Tauc's relation using Kubelka-Munk [K-M or F(R)] relation [46,47,48]:

$$\alpha = \ln [(R_{max} - R_{min}) / (R - R_{min})] \quad (1-2)$$

where R_{max} and R_{min} are the maximum and minimum values of reflectance, R is the reflectance at a given photon energy, hv . Figure 2.8 shows the reflection spectra of the c -Si compared with the PS Samples (left) and the extrapolation of a straight line using K-M relation for indirect allowed transition of the samples with different etching current densities A) 10 mA/cm², B) 20 mA/cm², and C) 30 mA/cm² (right) [46].

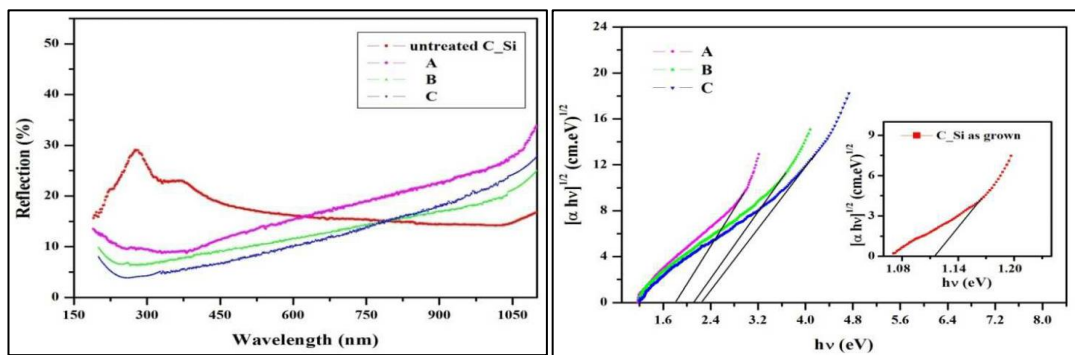


Figure 2.8: Reflection Spectra of the c -Si compared with the PS Samples (left) and the extrapolation of a straight line using K-M relation for indirect allowed transition of the samples with different etching current densities A) 10 mA/cm², B) 20 mA/cm², and C) 30 mA/cm² (right) [46].

2.3 Introduction of ZnO

ZnO is intrinsically *n*-type semiconductors with a wide direct band gap of 3.37 eV and a large exciton binding energy of 60 meV. ZnO have unique optical properties, high mechanical and thermal stabilities, and electronic properties [50]. ZnO has high sensitivity to UV light, high density of surface trap states and the much higher surface-area-to-volume ratio can improve the properties of photodetectors [51].

2.3.1 Background of ZnO

ZnO was created as a product by a process involving heating and melting (smelting) [52]. This smelting technique was then taken to China in the 16th or 17th century, to produce brasses with high zinc contents. Europeans imported zinc from China and later it was listed as an element on the periodic table in 1789 by Antoine Lavoisier [53]. The first electronic application of ZnO was built as a compartment in a radio sets in 1920. By in contact with ZnO crystal and a copper wire, a Schottky barrier was created and providing the rectification to convert the AC to DC [54].

2.3.2 Structural Properties of ZnO

Group II-VI are compound semiconductors (ZnO, ZnS, CdSe, CdTe), crystallize in cubic, zinc blende or hexagonal wurtzite structure where each anion is surrounded by four cations. Theoretically, ZnO can be scheming in the three phases of crystal structures either rock salt or Rochelle salt (B1), Zinc blende (B3) and Wurtzite (B4) as in Figure 2.9 [55].

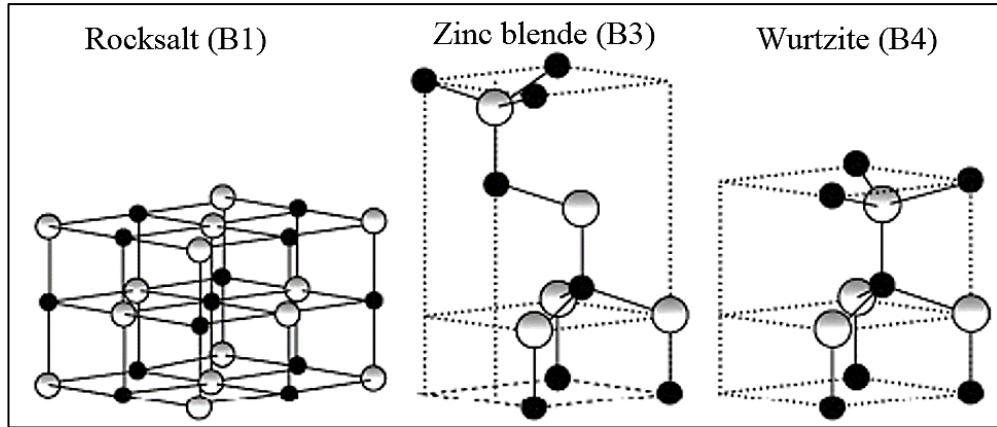


Figure 2.9: ZnO crystal structures, the small and big dot represent O and Zn atom, (a) cubic rock salt (B1), (b) cubic zinc blende (B3) and (c) hexagonal wurtzite (B4) [55].

ZnO is an intrinsic n -type semiconductor. It naturally crystallizes in the hexagonal wurtzite structure [56]. The hexagonal lattice in which each Zn^{2+} ion is tetrahedrally bonded to four O^{2-} ions and vice-versa. ZnO has two lattice parameters c and a in the ratio of 1.633, indicate an ideal wurtzite structure. In this structure, the Zn terminated face (0001) and O terminated face $(000\bar{1})$ are the polar faces while the non-polar faces are $(11\bar{2}0)$ and $(10\bar{1}0)$ which contain equal number of Zinc and Oxygen atoms. The plane perpendicular to the c -axis are called basal planes. The tetrahedral coordination of ZnO indicates the sp^3 hybridized covalent bonding, but the strong ionic character of the Zn-O bond, makes ZnO behave like both covalent and ionic compound. The bulk parameters of ZnO are calculated to be $a = 3.284 \text{ \AA}$ and $c = 5.333 \text{ \AA}$ [57] and also reported by Matthias and Diebold, lattice parameters of a , $b = 3.25 \text{ \AA}$, and $c = 5.206 \text{ \AA}$ [56]. There is a polar symmetry along the hexagonal axis and gives rise to piezoelectricity in ZnO [58]. Crystal structure simply shown in Figure 2.10. In ZnO, normally point defect (oxygen vacancy or Zn interstitial) gives high effects, can create electronic states in the band gap which influence its optical and electrical properties [58].